

Particle-continuum-medium duality of skyrmions

X. R. Wang^{1,2,3,*} and X. C. Hu^{1,2}

¹*Physics Department, The Hong Kong University of Science and Technology, Clear Water Bay, Kowloon, Hong Kong*

²*HKUST Shenzhen Research Institute, Shenzhen 518057, China*

³*William Mong Institute of Nano Science and Technology,*

The Hong Kong University of Science and Technology, Clear Water Bay, Kowloon, Hong Kong, China

(Dated: May 5, 2023)

Topological solitons are crucial to many branches of physics, such as models of fundamental particles in quantum field theory, information carriers in nonlinear optics, and elementary entities in quantum and classical computations. Chiral magnetic materials are a fertile ground for studying solitons. In the past a few years, a huge number of all kinds of topologically protected localized magnetic solitons have been found. The number is so large, and a proper organization and classification is necessary for their future developments. Here we show that many topological magnetic solitons can be understood from the duality of particle and elastic continuum-medium nature of skyrmions. In contrast to the common belief that a skyrmion is an elementary particle that is indivisible, skyrmions behave like both particle and continuum media that can be tore apart to bury other objects, reminiscing particle-wave duality in quantum mechanics. Skyrmions, like indivisible particles, can be building blocks for cascade skyrmion bags and target skyrmions. They can also act as bags and glues to hold one or more skyrmions together. The principles and rules for stable composite skyrmions are explained and presented, revealing their rich and interesting physics.

I. INTRODUCTION

Magnetic skyrmions have attracted much attention in recent years for their academic interest and potential applications in information technology [1–8]. Various aspects of magnetic skyrmions have been extensively and intensively studied [9–43], including characterization, generation, and manipulations. Recently, it was realized that only skyrmions with positive formation energy are intrinsically circular [44–47]. The natural morphology of skyrmions of negative formation energy are stripes of well-defined width. In this case, condensed stripy skyrmions, ranging from irregular maze to periodically arranged helical states, is the preferred thermodynamic equilibrium state [47]. Randomly or orderly arranged condensed stripe skyrmions transform into skyrmion crystals (SkXs) smoothly and continuously as stripe width increases via material parameter engineering [48] or as the skyrmion density increases through thermal agitations and/or the assistances of external forces [46, 47].

With all these advances in skyrmion physics, there are still many unsolved problems. For example, other than different elementary skyrmions mentioned above, in the past eight years, many localized magnetic structures, topologically different from the elementary skyrmions and with arbitrary integer skyrmion numbers, were found [49–71]. Skyrmionium, a spin texture of one skyrmion inside another larger skyrmion with zero net skyrmion number, have been observed both numerically and experimentally [49–58]. A skyrmionium can also be embedded inside another even larger skyrmion to form a

target skyrmion of 3 layers with net skyrmion number 1. In fact, this cascade process can continue to form target skyrmions of any cascade levels with skyrmion number 0 or 1 for even and odd numbers of layers, respectively. Target skyrmions cannot be continuously transformed into a single ferromagnetic domain structure or an elementary skyrmion. Also, so-called skyrmion bags, spin structures of arbitrary number of skyrmions inside another larger skyrmion, have also been observed [49, 59–64]. Their skyrmion numbers can be arbitrary integers Q and they cannot be continuously deformed into Q spatially separated elementary skyrmions. Similar to the target skyrmions, one can put one or many skyrmion bags into another even bigger skyrmion to form a cascade skyrmion bag of 3 layers. The process can also continue to have various cascade skyrmion bags of arbitrary layers. Although composite skyrmions have been found in various simulations and experiments, there is no clear understanding of their existence conditions. They were found through trial and error or hunch so far.

The increasing number of newly discovered topologically non-trivial localized spin structures in chiral magnetic films reminisces the discovery of a huge number of elementary particles in the first half of last century that resulted in the quark model of elementary particles. It calls for a “quark model” to properly organize these newly discovered topological magnetic structures. In this paper, we consider a perpendicularly magnetized chiral magnetic film with the Dzyaloshinskii–Moriya interaction (DMI) and normal ferromagnetic exchange interaction characterized by parameter D and A , respectively, as well as magnetic anisotropy measured by K . We show that the stability and properties of various types of composite skyrmions is very sensitive to a parameter defined as $\kappa \equiv (\pi D)^2 / (16AK)$. Near $\kappa = 1$ that separates isolated circular skyrmions from condensed stripe skyrmions [45],

* Electronic address: phxwan@ust.hk

the skyrmions show strong particle-continuum-medium duality. In contrast to the general belief that a skyrmion is a fundamental object indivisible. A skyrmion behaves sometimes like a continuum medium that can be tore apart to embed one or more than one skyrmions or composited skyrmions although it often appears as a particle. In another word, one or many circular and stripe skyrmions can be hold or be glued by another larger skyrmion, which acts as a glue or a bag, to form a skyrmionium or skyrmion bag/cluster. The embedding can continue layer by layer to form all kinds of target skyrmions and cascade skyrmion bags.

Specifically, following interesting results were obtained in the absence of the external magnetic field for $\kappa \leq 1$ where isolated circular skyrmions are metastable and $\kappa > 1$ where condensed stripe skyrmions are stable. 1) Topologies of stable static magnetic textures are fully determined by κ , and A/D defines their length scale. 2) The maximal number of cascade layers in target skyrmions for $\kappa \leq 1$ increases monotonically from 1 at $\kappa = 0.7$, to 2 at $\kappa = 0.8$, and to 4 at $\kappa = 0.94$, and eventually diverges at $\kappa = 1$ for an infinite large system. 3) An unstable target skyrmion or skyrmion bag for $\kappa < 1$ can be stabilized by inserting enough skyrmions inside the innermost bag and/or the next innermost bag. The maximal number of skyrmions needed to stabilize a skyrmion bag decreases from a larger value at small κ , say 4 at $\kappa = 0.7$, to the lowest possible 1 when κ approaches 1. This number increases also as the number of cascade layers increases. Furthermore, skyrmion size inside the innermost bag increases with the number of skyrmions inside the bag, and approaches the size of isolated elementary skyrmions. 4) For $\kappa > 1$, the number of target stripe skyrmions and cascade stripe skyrmion bags can be any number as long as the average space-size occupied by each skyrmion is larger than twice of elementary stripe width. Furthermore, stripe width and stripe spin profile of any target stripe skyrmions and cascade stripe skyrmion bags are the same as those of elementary stripe skyrmions. 5) When the average skyrmion-skyrmion distance inside a stripe skyrmion bag is comparable to the elementary stripe width for $\kappa > 1$, stripe skyrmions in the innermost layer become disk-like objects and form an SkX. The paper is organized as follows. The model and methodology is present in the next section. We prove there that stable/metastable spin structures are fully determined by κ with the fundamental length scale of $4A/(\pi D)$. Section III is the results, and discussion and conclusion are given in Sec. IV.

II. MODEL AND METHODOLOGY

To demonstrate particle-continuum-medium duality of skyrmions, we consider a thin chiral magnetic film of thickness d in the xy-plane. The magnetic energy of a

spin structure \vec{m} is

$$E = d \iint \{A|\nabla\vec{m}|^2 + D[(\vec{m} \cdot \nabla)m_z - m_z\nabla \cdot \vec{m}] + K_u(1 - m_z^2) - \frac{1}{2}\mu_0 M_s \vec{H}_d \cdot \vec{m} + \mu_0 H M_s(1 - m_z)\} dS, \quad (1)$$

where K_u , H , M_s , \vec{H}_d and μ_0 are the magneto-crystalline anisotropy, perpendicular magnetic field, the saturation magnetization, the demagnetizing field and the vacuum permeability, respectively. The energy of ferromagnetic state $m_z = 1$ is chosen as the energy reference of $E = 0$. For an ultra thin film, demagnetization effect can be included in the effective anisotropy $K = K_u - \mu_0 M_s^2/2$. This is a good approximation when the film thickness d is much smaller than the exchange length [9].

One can recast Eq. (1) to reveal how model parameters affect stable/metastable magnetic structures,

$$\begin{aligned} E &= d \iint \{A|\nabla\mathbf{m}|^2 + D[m_z\nabla \cdot \mathbf{m} - (\mathbf{m} \cdot \nabla)m_z] \\ &\quad + K(1 - m_z^2) + \mu_0 H M_s(1 - m_z)\} dx dy \\ &= d\kappa K \iint \{L|\nabla\mathbf{m}|^2 + \frac{4L}{\pi}[m_z\nabla \cdot \mathbf{m} - (\mathbf{m} \cdot \nabla)m_z] \\ &\quad + \frac{1}{\kappa}(1 - m_z^2) + \frac{2}{\kappa'}(1 - m_z)\} dx dy \\ &= dA \iint \{|\nabla\mathbf{m}|^2 + \frac{4}{\pi}[m_z\nabla \cdot \mathbf{m} - (\mathbf{m} \cdot \nabla)m_z] \\ &\quad + \frac{1}{\kappa}(1 - m_z^2) + \frac{2}{\kappa'}(1 - m_z)\} dx dy, \end{aligned} \quad (2)$$

where $\kappa = \frac{\pi^2 D^2}{16AK}$, $\kappa' = \frac{\pi^2 D^2}{8A\mu_0 M_s H}$, and $L = 4A/(\pi D)$. The stable/metastable spin structures minimize the last integral of above equation [47] where x and y is in the units of L . In the absence of external magnetic field ($1/\kappa' = 0$) considered here, all stable/metastable magnetic structures satisfy following dimensionless equation,

$$\nabla^2 \vec{m} + \frac{4}{\pi} [(\nabla \cdot \vec{m})\hat{z} - \nabla m_z] + \frac{1}{\kappa} m_z \hat{z} = 0. \quad (3)$$

In another word, stable/metastable magnetic structures are fully determined by κ , not by A , D , M_s , and K separately. L is the length scale. This fact greatly simplifies our study of skyrmion static properties, and all stable magnetic structures in general. It allows us to compare skyrmions in different chiral magnets in terms of κ . Varying κ over all possible values corresponds to studying all possible magnetic films. Isolated circular skyrmions are metastable and their energies are $E = 8\pi A d \sqrt{1 - \kappa}$ when $H = 0$ and $\kappa \leq 1$ [9]. Obviously, the formation energy of an isolated skyrmion goes to zero as κ approaches 1. Earlier studies [44–47] showed that $\kappa = 1$ separates isolated circular skyrmions from condensed stripe skyrmions. The natural skyrmion morphologies are stripes in order to take the advantages of negative skyrmion formation energy when $\kappa > 1$ [46].

Spin dynamics in a magnetic field is governed by the Landau-Lifshitz-Gilbert (LLG) equation,

$$\frac{\partial \vec{m}}{\partial t} = -\gamma \vec{m} \times \vec{H}_{\text{eff}} + \alpha \vec{m} \times \frac{\partial \vec{m}}{\partial t}, \quad (4)$$

where γ and α are respectively gyromagnetic ratio and Gilbert damping constant. $\vec{H}_{\text{eff}} = \frac{2A}{\mu_0 M_s} \nabla^2 \vec{m} + \frac{2K_u}{\mu_0 M_s} m_z \hat{z} + H \hat{z} + \vec{H}_d + \vec{H}_{\text{DM}} + \vec{h}$ is the effective field which includes the exchange field, the anisotropy field, the external magnetic field along \hat{z} , the demagnetizing field, the DMI field \vec{H}_{DM} , and the thermal fluctuating field \vec{h} (in the case of finite temperature), respectively [72]. In the absence of an energy source, the steady state solutions of Eq. (4) are stable/metastable spin textures. We will use MuMax3 [72] to obtain all kinds of composite skyrmions. The initial configurations are important in this endeavour. According to our previous study [44], each nucleation domain in a chiral magnetic film, in which skyrmions are stable/metastable, develops into a skyrmion. Thus, various domains embedded inside other domains can develop into various composite skyrmions, as demonstrated below.

III. RESULTS

A. Target skyrmions and cascade skyrmion bags at $\kappa = 0.9$ and $\kappa = 4$

Stable/metastable composite skyrmions are expected to more favourably appear in chiral magnetic films with κ slightly smaller than 1 or $\kappa > 1$ because creating an individual skyrmion gains energy for $\kappa > 1$ and costs nearly zero energy near $\kappa = 1^-$. To demonstrate that this expectation is indeed true, we choose $A = 4 \text{ pJ m}^{-1}$, $D = 1 \text{ mJ m}^{-2}$, and $M_s = 0.15 \text{ MA m}^{-1}$, values in the range of $A = 2 \sim 16 \text{ pJ m}^{-1}$, $D = 0.68 \sim 4 \text{ mJ m}^{-2}$, $K_u = 0.2 \sim 2.5 \text{ MJ m}^{-3}$ and $M_s = 0.65 \sim 1.1 \text{ MA m}^{-1}$ for chiral magnets of Ir/Fe/Co/Pt multilayer and PdFe/Ir bilayers [8, 24, 29, 73]. K_u is used to simulate samples with different κ since in reality K_u is sensitive to chemical compositions, fabrication process, structures, and the temperature. $K_u = 0.185 \text{ MJ m}^{-3}$ and $K_u = 0.0526 \text{ MJ m}^{-3}$ give $\kappa = 0.9$ and $\kappa = 4$, respectively. As explained in the previous section, the stable/metastable structures for the same κ are invariant when they are scaled by $4A/(\pi D)$. Figure 1 shows the typical structures of composite skyrmions in a sample of $400 \text{ nm} \times 400 \text{ nm} \times 0.5 \text{ nm}$ in size with periodic boundary conditions along both x and y directions. Throughout this study, skyrmion structures are encoded in the gray-scale for m_z and by colors for skyrmion charge density ρ defined as $\rho = \mathbf{m} \cdot (\partial_x \mathbf{m} \times \partial_y \mathbf{m}) / (4\pi)$.

Figure 1(a1) is a stable skyrmionium, starting from an initial configuration of a $30 \text{ nm} \times 30 \text{ nm} \times 0.5 \text{ nm}$ ($m_z = -1$)-domain inside another ($m_z = 1$)-domain of $100 \text{ nm} \times 100 \text{ nm} \times 0.5 \text{ nm}$ at the center in the background

of $m_z = -1$ as shown in the inset (the red-line square). It forms shortly a stable skyrmionium of skyrmion number (charge) 0 with an inner core of topological charge -1 and an outer shell of topological charge 1, separated by the white-color circle on which $\rho = 0$. The topological charge remains 0 shortly after 10 ps as shown by the black solid curve in Fig. 1(c). Figure 1(a2) is a stable composite topological skyrmion with two skyrmions inside another larger skyrmion, starting from an initial configuration (shown in the inset) of two $30 \text{ nm} \times 30 \text{ nm} \times 0.5 \text{ nm}$ ($m_z = -1$)-domains inside another ($m_z = 1$)-domain of $100 \text{ nm} \times 100 \text{ nm} \times 0.5 \text{ nm}$ in the background of $m_z = -1$. Two skyrmions enclosed by the white-color contour of $\rho = 0$ have skyrmion number -1 each while the total charge outside of the contour is 1. The red solid curve in Fig. 1(c) is the time evolution of the total topological charge $Q(t)$, $Q(t) = -1$ shortly after 10 ps evolution. Similarly, Fig. 1(a3) is a stable cascade skyrmion bag of 3 cascade layers: two composite skyrmions shown in Fig. 1(a2) inside another larger skyrmion. This cascade skyrmion bag comes from an initial configuration consisting of two composite domains as that in the inset of Fig. 1(a2) inside another larger domain. As expected, this composite skyrmion has a skyrmion number of $4 \times (-1) + 2 \times 1 + (-1) = -3$ as shown by the blue curve in Fig. 1(c). Interestingly, $Q(t)$ exhibits a peak with a positive value larger than 1 before reaching its final negative value and its cause is unknown yet.

In order to investigate whether the above results are also true for stripe skyrmions when skyrmion formation energy is negative, we repeat the above simulations for film with $\kappa = 4$. Figures 1(b1)-(b3) show three stable structures of composite stripe skyrmions: stripe skyrmionium of topological charge 0 or one stripe skyrmion inside another larger stripe skyrmion (b1); a composite stripe skyrmion bag of topological charge -1 with two stripe skyrmions inside another larger stripe skyrmions (b2); a composite cascade stripe skyrmion bag of topological charge -3 with two composite stripe skyrmion bags as shown in Fig. 1(b2) inside another stripe skyrmions (b3). As a direct comparison to the case of $\kappa = 0.9$, the initial configurations are exactly the same as their corresponding counterparts in Figs. 1(a1)-(a3). The dash curves in Fig. 1(c) are the time evolution of topological charge of different structures. Different from the case of $\kappa < 1$, $Q(t)$ reaches monotonically to its final stable values. Also, different from the case of $\kappa < 1$ where the skyrmion sizes in different layers are different, the stripe width in the current case are the same. Even more interestingly, spin profile are the same as that for elementary stripe skyrmion [45], $\Theta(x) = 2 \arctan\left[\frac{\sinh(L/w)}{\sinh(x/w)}\right]$ for $m_z > 0$ and $\Theta(x) = 2 \arctan\left[\frac{\sinh(x/w)}{\sinh(L/w)}\right]$ for $m_z < 0$, respectively, with $|x| \leq L/2$. Θ is the polar angle of the magnetization at x and $x = 0$ is the center of a stripe where $m_z = \pm 1$. The symbols in Fig. 1(d) are numerical data along the green line labelled by green $\textcircled{1}$ in Figs. 1(b1)-(b3). The solid curve is the fit of spin profiles to

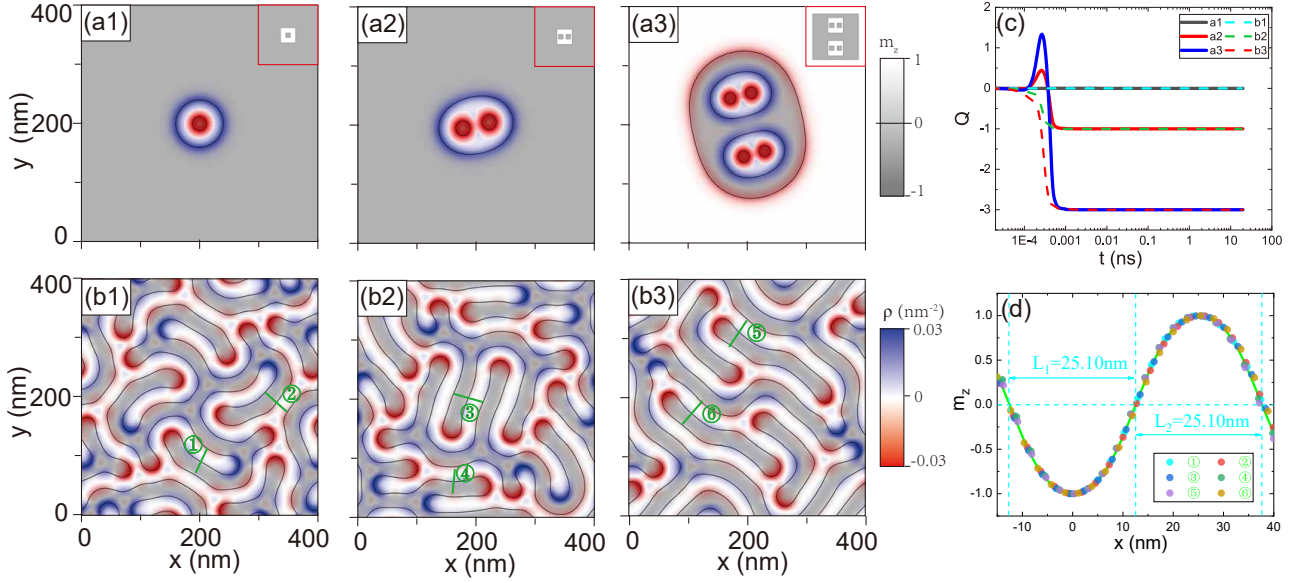


FIG. 1. Typical structures and profiles of composite circular skyrmions for $\kappa = 0.9$ (a1)-(a3) and composite stripe skyrmions for $\kappa = 4$ (b1)-(b3). One skyrmion inside another one (a1) and (b1) from the same initial configuration shown in the inset of (a1); two skyrmions inside another larger one (a2) and (b2) from the initial configuration shown in the inset of (a2); two composite skyrmions of (a2) or (b2) inside another larger skyrmion (a3) and (b3) from the initial configuration shown in the inset of (a2). (c) Time evolution of topological charges for structures (a1) (the black solid line); (a2) (the red solid line); (a3) (the blue solid line); (b1) (the cyan dash line); (b2) (the green dash line); and (b3) (the red dash line). t is in the logarithmic scale. Skyrmion charge density ρ is encoded by colours (the blue for positive and the red for negative) while the gray-scale encodes m_z . (d) Spin profiles $m_z(x)$ along the green lines labelled by ① in (b1)-(b3). The symbols are numerical data and the solid lines are the theoretical fits to $\cos \Theta(x) = -\frac{\sinh^2(L/2w) - \sinh^2(x/w)}{\sinh^2(L/2w) + \sinh^2(x/w)}$ for $-L/2 < x < L/2$ and $\cos \Theta(x) = \frac{\sinh^2(L/2w) - \sinh^2[(x-L)/w]}{\sinh^2(L/2w) + \sinh^2[(x-L)/w]}$ for $L/2 < x < 3L/2$ with $L = 25.10$ nm and $w = 7.63$ nm.

$\cos \Theta(x) = -\frac{\sinh^2(L/2w) - \sinh^2(x/w)}{\sinh^2(L/2w) + \sinh^2(x/w)}$ for $-L/2 < x < L/2$
and $\cos \Theta(x) = \frac{\sinh^2(L/2w) - \sinh^2[(x-L)/w]}{\sinh^2(L/2w) + \sinh^2[(x-L)/w]}$ for $L/2 < x < 3L/2$ with $L = 25.10$ nm and $w = 7.63$ nm. All data from different stripes falling onto the same curve demonstrates that stripes, building blocks of the pattern, are identical.

B. Maximal layer number of target skyrmions for $\kappa \leq 1$

TABLE I. The value of material parameters K , K_u and κ for 8 different films.

Films	K_u (MJ m ⁻³)	K (MJ m ⁻³)	κ
1	0.2344	0.2203	0.7
2	0.2197	0.2056	0.75
3	0.2068	0.1927	0.8
4	0.1955	0.1814	0.85
5	0.1854	0.1713	0.9
6	0.1817	0.1676	0.92
7	0.1781	0.1640	0.94
8	0.1747	0.1606	0.96

When $\kappa < 1$, the skyrmion formation energy of an elementary skyrmion is $E = 8\pi A\sqrt{1 - \kappa}$ [9], and skyrmion

size and skyrmion wall width are $R = \pi D / (4K\sqrt{1 - \kappa})$ and $w = \pi D / (4K)$, respectively. The energy cost is mainly from the skyrmion wall region. The size and wall regions in a composite skyrmion is obviously larger than that in an elementary skyrmion, resulting in an increase of energy-cost. Thus, stability of various composite skyrmions should be sensitive to how far κ is away from 1 at which the energy cost for creating a wall is zero. Although an isolated skyrmion is expected to be metastable when $\kappa < 1$ as long as the skyrmion size is much bigger than the lattice constant a , $R > a$ or $\kappa > 1 - [\pi D / (4Ka)]^2$, in order to validate the continuum description of the films by Eqs. (1), (2), and (3), the maximal number of cascade layers of target skyrmions should change with κ . In order to test this hypothesis, we consider 8 samples with various K_u listed in Tab. I while all other model parameters are unchanged. The corresponding κ values are 0.7, 0.75, 0.8, 0.9, 0.92, 0.94 and 0.96. We started with a cascade domain-inside-domain structure as shown in Fig. 2(b), consisting of 6 white ($m_z = 1$)-domains and 6 gray ($m_z = -1$)-domains. They were segregated by 11 concentric squares of side lengths of 750, 700, 650, 600, 550, 500, 450, 400, 350, 300, 250 nm at the film center. The sample size is of 2400 nm \times 2400 nm \times 0.5 nm, large enough so that the final stable spin structures do not depend on the

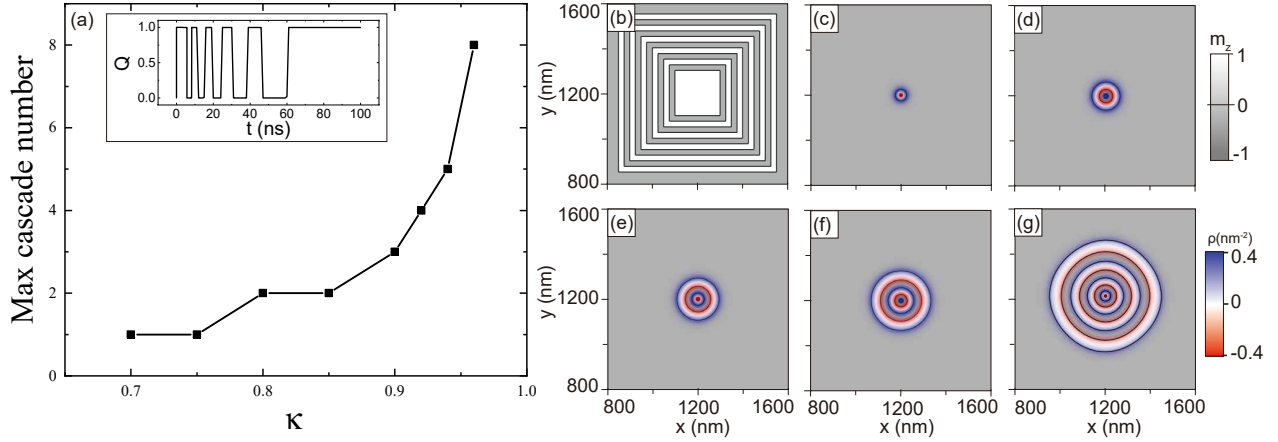


FIG. 2. (a) κ -dependence of the maximal number of layers of target skyrmions. The inset shows how skyrmion number of unstable composite spin structure varies with time t when $\kappa = 0.7$. The final stable spin texture is an elementary skyrmion of $Q = 1$. (b) The initial configuration of a cascaded domain-inside-domain structure of $n = 11$. (c)-(g) The final metastable target skyrmions from the initial configuration of (b) for various κ : Skyrmionium for $\kappa = 0.8$ (c) and target skyrmions of 3 layers for $\kappa = 0.9$ (d), of 4 layers for $\kappa = 0.92$ (e), of 5 layers for $\kappa = 0.94$ (f), and of 8 layers for $\kappa = 0.96$ (g). Color bar denotes skyrmion charge density and the gray-scale encodes m_z .

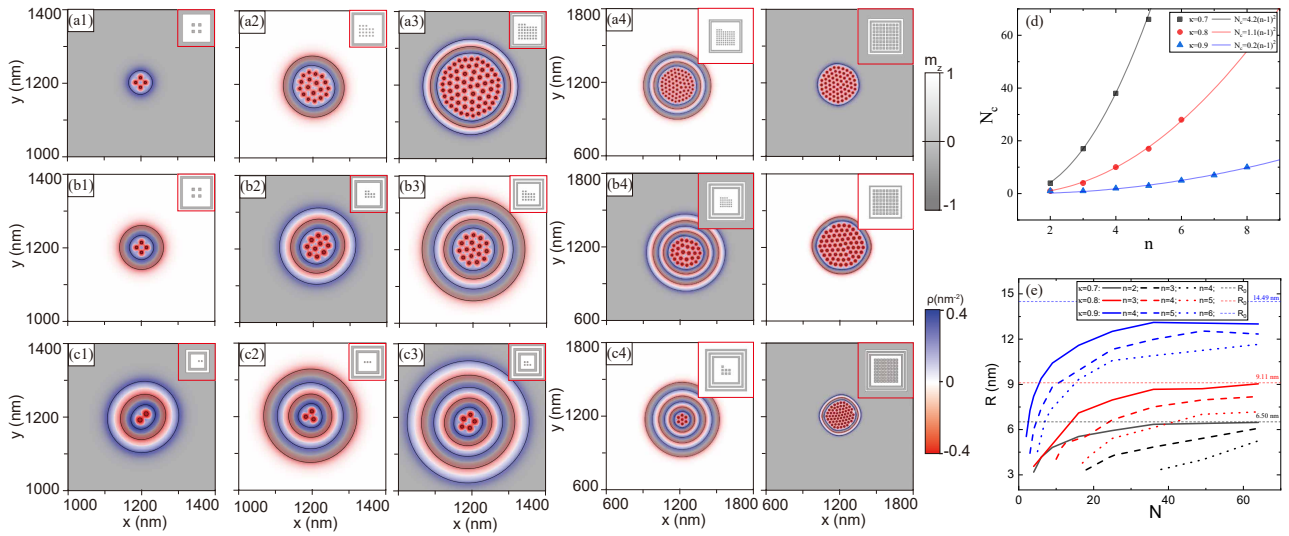


FIG. 3. Various stable cascade skyrmion bags of $n = 2, 3, 4$, and 5 cascade layers for $\kappa = 0.7, 0.8$, and 0.9 . (a1)-(a4) Stable cascade skyrmion bags of $n = 2, 3, 4$, and 5 layers with minimal number of $N_c = 4$ (a1), 18 (a2), 38 (a3), and 66 (a4) skyrmions in the innermost bag for $\kappa = 0.7$. (a5) A stable skyrmion bag of $N = 64 \gg N_c$ and $n = 2$ for $\kappa = 0.7$. (b1)-(b4) Stable cascade skyrmion bags of $n = 3, 4, 5$, and 6 layers with minimal number of $N_c = 4$ (b1), 10 (b2), 17 (b3), and 28 (b4) skyrmions in the innermost bag for $\kappa = 0.8$. (b5) A stable cascade skyrmion bag of $N = 64 \gg N_c$ and $n = 3$ for $\kappa = 0.8$. (c1)-(c4) Stable cascade skyrmion bags of $n = 4, 5, 6$ and 7 layers with minimal number of $N_c = 2$ (c1), 3 (c2), 5 (c3), and 7 (c4) in the innermost bag for $\kappa = 0.9$. The insets are the initial configurations. (c5) A stable cascade skyrmion bag of $n = 4$ and $N = 64 \gg N_c$ skyrmions in the innermost bag for $\kappa = 0.9$. (d) N_c vs. n . Dots are numerical data for $\kappa = 0.7$ (the black); 0.8 (the red) and 0.9 (the blue). The solid lines are the fits of data to $N_c = a(\kappa)(n - 1)^2$, with $a(0.7) = 4.2$, $a(0.8) = 1.1$, and $a(0.9) = 0.2$. (e) Skyrmion size in the innermost bag as a function of the number of skyrmions N in the innermost bag for $\kappa = 0.7$ and $n = 2$ (the black full line); $\kappa = 0.7$ and $n = 3$ (the black dash line; $\kappa = 0.7$ and $n = 4$ (the black point line); $\kappa = 0.8$ and $n = 3$ (the red full line); $\kappa = 0.8$ and $n = 4$ (the red dash line); $\kappa = 0.8$ and $n = 5$ (the red point line); $\kappa = 0.9$ and $n = 4$ (the blue full line); $\kappa = 0.9$ and $n = 5$ (the blue dash line); $\kappa = 0.9$ and $n = 6$ (the blue point line) and elementary skyrmion size for $\kappa = 0.7$ (the black short dash line); $\kappa = 0.8$ (the red short dash line); $\kappa = 0.9$ (the blue short dash line). Color bar denotes skyrmion charge density and the gray-scale encodes m_z .

sample size. The mesh size is $1\text{ nm} \times 1\text{ nm} \times 0.5\text{ nm}$ in the simulations. For $\kappa = 0.7$, the initial configuration quickly evolves into an unstable shell structure of skyrmions number $Q = 1$ in less than 10 ps as shown in the inset of Fig. 2(a) in the first jump around $t = 0$ from $Q = 0$ to 1 in $Q(t)$ - t curve. Simulations show that the shell structure shrinks its size, and the innermost spin structure disappears one by one from the center. As revealed in $Q(t)$ - t curve, Q jumps back and forth between 1 and 0 each time when one shell disappears. The final metastable spin structure is an elementary skyrmion of $Q = 1$, indicating that target skyrmions and skyrmionium are not stable when $\kappa = 0.7$.

For $\kappa = 0.8$, the final stable spin structure is a skyrmionium as shown in Fig. 2(c). Figures 2(d)-(g) are the final stable target skyrmions for $\kappa = 0.9, 0.92, 0.94$, and 0.96 with maximal layer number 3 (d), 4 (e), 5 (f), and 8 (g), respectively. The κ -dependence of the maximal number of cascade layers in the final stable/metastable target skyrmions is plotted in Fig. 2(a), showing the number increases to a very large value as κ approaches 1.

C. Stabilization and properties of cascade skyrmion bags for $\kappa \leq 1$

Figure 2 shows the maximal number of layers in stable target skyrmions being 1 for $\kappa = 0.7$, i.e. even a skyrmionium of $Q = 0$ is not stable. The energy of a skyrmion bag with many skyrmions in the innermost layer is higher than that of a skyrmionium. Thus, one may expect that a spin bag is more unstable than a skyrmionium for $\kappa = 0.7$. Surprisingly and counter-intuitively, skyrmion bags with N skyrmions inside another larger skyrmion are stable as long as N is larger than a critical value of $N_c = 4$ as shown in Fig. 3(a1) for $N = N_c = 4$ and in Fig. 3(a5) for $N = 64$. Their total net topological charges are respectively $Q = -3$ and $Q = -63$ obtained from the initial configurations of 4 and 64 ($m_z = -1$)-domains inside a ($m_z = 1$)-domain as shown in the insets. Similarly, the cascade skyrmion bags of n layers can also be stabilized by putting N skyrmions in the innermost bag when N is larger than a critical value $N_c(n)$ which depends on layer number of cascade skyrmion bag. Figures 3(a2)-(a4) are the stable cascade skyrmion bags of $n = 3, 4$ and 5 with corresponding $N_c = 18, 38$ and 66 when $\kappa = 0.7$ respectively. These cascade skyrmion bags are obtained from the initial configurations shown in the insets. The net topological charges of these cascade skyrmion bags are $Q = -18, -37$ and -66 . For $\kappa = 0.8$, Figs. 3(b1)-(b4) show cascade skyrmion bags of $n = 3, 4, 5$ and 6 with corresponding $N_c = 4, 10, 17$ and 28 . Figure 3(b5) shows a stable cascade skyrmion of 3 layers with $N = 64$ which is larger than $N_c = 4$. For $\kappa = 0.9$, Figs. 3(c1)-(c4) show cascade skyrmion bags of $n = 4, 5, 6$ and 7 with corresponding $N_c = 2, 3, 5$ and 7 . Figure 3(c5) shows a stable cascade skyrmion of 3 layers with $N = 64$ which is larger

than $N_c = 2$.

Interestingly, we find that N_c is proportion to $(n-1)^2$ for all our κ 's. Figure 3(d) shows the relation between N_c and n for $\kappa = 0.7$ (black dots); 0.8 (red dots) and 0.9 (blue dots). Numerical data (symbols) fit well to $N_c = 4.2(n-1)^2$ (the black line); $N_c = 1.1(n-1)^2$ (the red line); $N_c = 0.2(n-1)^2$ (the blue line). More interestingly, the skyrmion size R of skyrmions in the innermost bag is smaller than that of elementary skyrmions, $R_0 = \pi D / (4K\sqrt{1-\kappa})$, but it increases with N as shown in Fig. 3(e).

In order to explain why a cascade skyrmion bag at a lower κ , say $\kappa = 0.7$, needs a minimal number of skyrmions in the innermost bag to stabilize itself, one may suspect that innermost bag size needs to be large enough so that geometrical restriction would not annihilates the skyrmions in the bag. If this is correct, one would expect that adding more skyrmions to the next innermost bag tends to destabilize a cascade skyrmion bag because skyrmions in the next innermost bag tends to reduce innermost bag size. And minimal number of skyrmions in the innermost bag of a stable cascade skyrmions increases with number of skyrmions in the next innermost bag. Strangely, this seemingly reasonable conjecture turns out to be incorrect. Contrary to this conjecture, we find the opposite results. As shown in Fig. 4(a1) for a stable cascade skyrmion bag of 3 layers ($n = 3$) at $\kappa = 0.7$, the cascade skyrmion bag have 7 skyrmions in the innermost bag and 32 skyrmions in the next innermost bag. In Fig. 3(a2) we have seen that the minimal number of skyrmions in the innermost bag required to stabilize the cascade skyrmion is $N_c = 18$ if no extra skyrmions are in the next innermost bag. In fact, all cascade skyrmion bags with 7 skyrmions in the innermost bag are stable as long as the number of skyrmions in the next innermost bag is larger than 32. Figure 4(a4) shows a cascade skyrmion bag of 3 layers with 7 skyrmions in the innermost bag and 80 skyrmions in the next innermost bag. The minimal number of skyrmions in the next innermost bag decreases as the number of skyrmions in the innermost bag increases. Equivalently, the minimal number of skyrmions in the innermost bag decreases with the increase of the number of skyrmions in the next innermost bag. Figures 4(a2)-(a3) are two stable cascade skyrmion bags of 3 layers with 10 and 16 skyrmions in the innermost bag and corresponding minimal 18 and 2 skyrmions in the next innermost bag, respectively.

Above results are very sensitive to layer number n in cascade skyrmion bags. If one keeps the number of skyrmions in the innermost bag of a cascade skyrmion bag below its minimal value such that the composite skyrmion by itself is unstable, the minimal number of skyrmions in the next innermost bag $N_{1,c}(n)$ required to stabilize the cascade skyrmion bag increases with the cascade level. Figures 4(b1)-(b3) are stable cascade skyrmion bags of 4, 5, and 6 and layers with 16 skyrmions in the innermost bag and minimal 44, 104 and

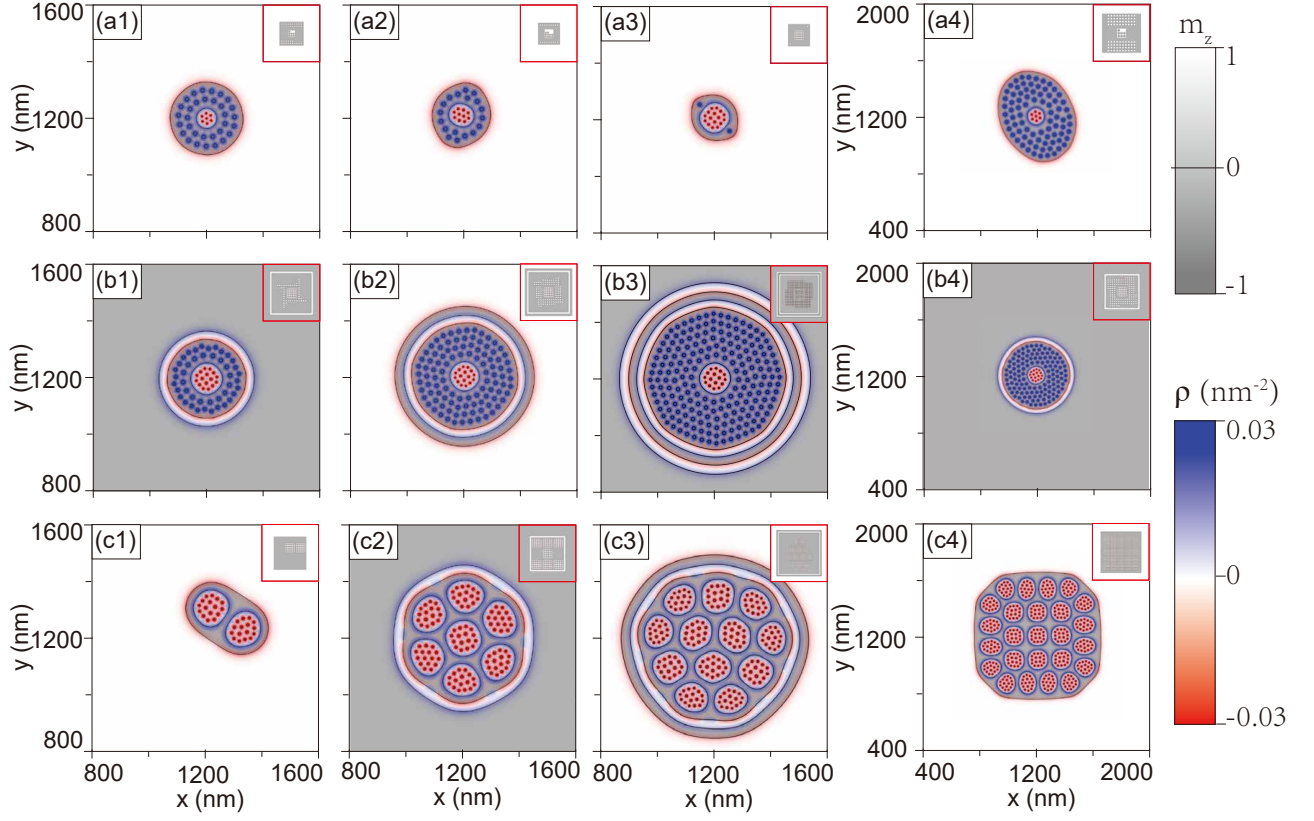


FIG. 4. Various composite skyrmion of $\kappa = 0.7$. (a1)-(a3) Stable cascade skyrmions of $N = 7$ and minimal $N_{1,c} = 32$ (a1); $N = 10$ and $N_{1,c} = 18$ (a2); $N = 16$ and $N_{1,c} = 2$ (a3). (a4) A stable cascade skyrmion of $N = 7$ and $N_1 = 80$ which is much larger than the critical value of 32. (b1)-(b3) Stable cascade skyrmion bags of $n = 4, 5$, and 6 layers and $N = 16$ and $N_{1,c} = 44, 104$, and 200. (b4) A stable cascade skyrmions of $n = 4$, $N = 10$, and $N_1 = 128$ which is much larger than the corresponding critical value of 44. (c1)-(c3) Four stable skyrmion superstructures of $n = 3, 4$, and 5 layers with minimal 2 (c1), 7 (c2), 12 (c3) skyrmion bags in the innermost layers. Each skyrmion bag contains $N = 16$ elementary skyrmions. (c4) A stable skyrmion superstructure of 3 layers with 25 skyrmion bags of $N = 16$. Color bar denotes skyrmion charge density and the gray-scale encodes m_z .

200 skyrmions in the next innermost bag, respectively. Figure 4(b4) is a stable cascade skyrmion of 4 layers of $N = 16$ and $N_1 = 128$ which is much larger than the corresponding critical value $N_{1,c} = 44$.

Instead of inserting elementary skyrmions into one particular cascade layer, one can also put skyrmion bags into it to obtain a more complicated skyrmion superstructure. Figures 4(c1)-(c3) are three such stable super skyrmion bags for $\kappa = 0.7$ where skyrmionium and other target skyrmions are unstable. Different from Fig. 3(a1) where adding 4 elementary skyrmions into an unstable skyrmionium can obtain a stable skyrmion bag, Fig. 4(c1) is a stable skyrmion superstructure when we insert two skyrmion bags of $N = 16$ into an unstable skyrmionium. Of course, this skyrmion superstructure has $n = 3$ cascade layers and the total skyrmion number is $2 \times (16 - 1) + 1 = 31$. 2 is the minimal number of bags needed to stabilise the structure. All skyrmion superstructures with more than 2 skyrmion bags in an unstable skyrmionium are stable, as shown in Fig. 4(c4) with 25 skyrmion bags of $N = 16$. The minimal number

of bags required to stabilize an unstable target skyrmion of more layers increases with the target skyrmion layers. Figures 4(c2) and (c3) are the final stable skyrmion superstructures when minimal 7 and 12 skyrmion bag of $N = 16$ are inserted into a target skyrmion of 3 (c2) and 4 (c3) layers, respectively. One notes that different sample sizes are used for these two cases in order to make sure that the results are not affected by the boundaries.

D. Resilience of stripe width of composite skyrmions for $\kappa > 1$

Skyrmions are stripes with negative formation energy when $\kappa > 1$, and fundamental stripe width is $a(\kappa)2\pi A/D$, where $a(\kappa)$ quickly and monotonically decreases from $+\infty$ at $\kappa = 1^+$ to 1 at $\kappa \gg 1$ [44, 45]. Thus, low energy states of a chiral magnetic film are condensed stripe skyrmions with the optimal stripe width. Different from the isolated skyrmions that cost energy to create skyrmion walls, stripes at low skyrmion density are flex-

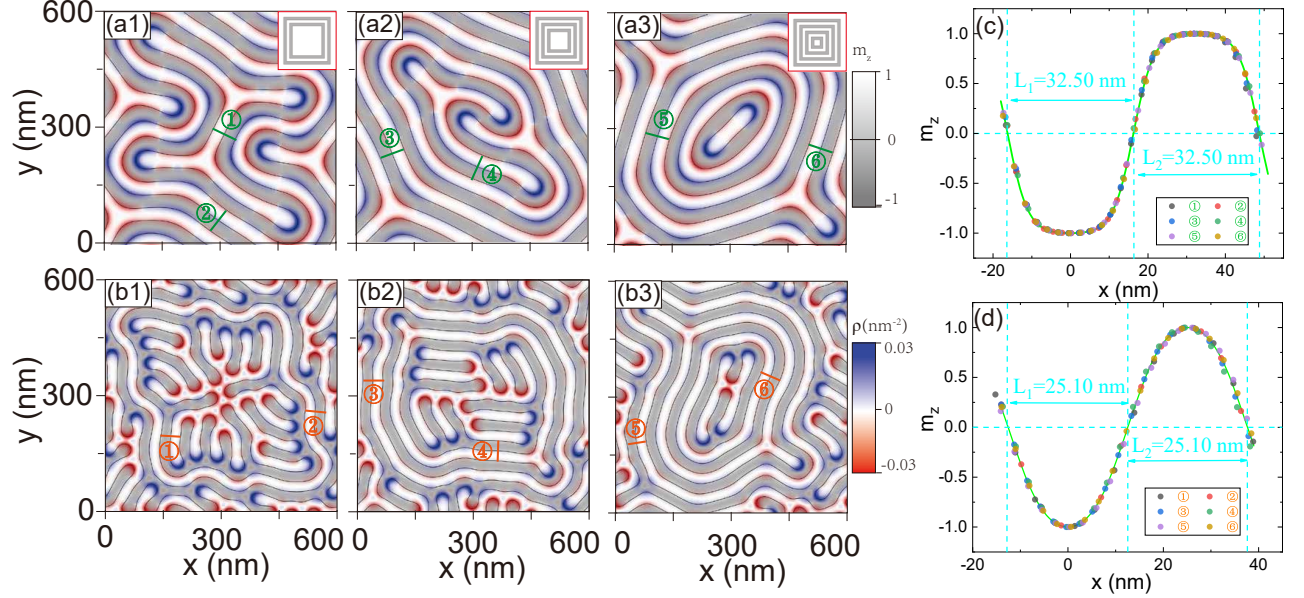


FIG. 5. Stable target stripe skyrmions of 4, 6, and 8 layers for $A/D = 4$ nm and $\kappa = 1.1$ (a1)-(a3) and $\kappa = 4$ (b1)-(b3), respectively. The sample sizes are $600 \text{ nm} \times 600 \text{ nm} \times 0.5 \text{ nm}$ and the average layer width is larger than the elementary strip width. (a1) and (b1), (a2) and (b2), and (a3) and (b3) start respectively from the same initial configurations shown in the inset of (a1) (a2), and (a3). (c)-(d) Spin profile of $m_z(x)$ along the green lines and orange line labelled by $\textcircled{1}$ in (a1)-(b3). The symbols are numerical data and the solid lines are the theoretical fits to $\cos \Theta(x) = -\frac{\sinh^2(L/2w) - \sinh^2(x/w)}{\sinh^2(L/2w) + \sinh^2(x/w)}$ for $-L/2 < x < L/2$ and $\cos \Theta(x) = \frac{\sinh^2(L/2w) - \sinh^2[(x-L)/w]}{\sinh^2(L/2w) + \sinh^2[(x-L)/w]}$ for $L/2 < x < 3L/2$ with $L = 32.50$ nm and $w = 5.23$ nm (c); and $L = 25.10$ nm and $w = 7.63$ nm (d). Color bar denotes skyrmion charge density and the gray-scale encodes m_z .

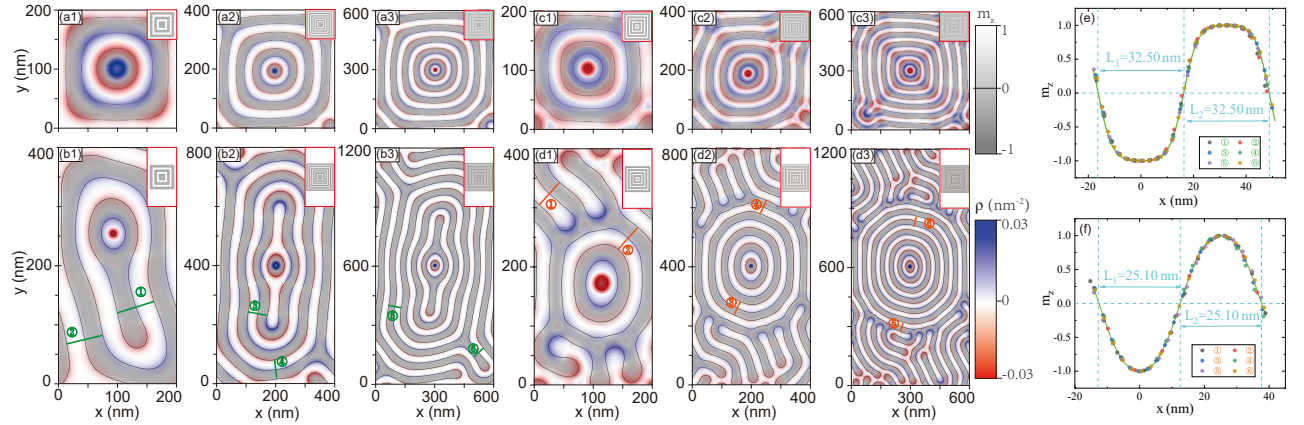


FIG. 6. Target stripe skyrmions with the maximal numbers of cascade layers n_{max} for $\kappa = 1.1$ and 4. The maximal numbers increase with sample sizes and are slightly larger than the ratio of sample size and the elementary stripe width. (a1)-(a3) Stable target skyrmions of $n_{max} = 4, 8$ and 11 in $200 \text{ nm} \times 200 \text{ nm} \times 0.5 \text{ nm}$, $400 \text{ nm} \times 400 \text{ nm} \times 0.5 \text{ nm}$ and $600 \text{ nm} \times 600 \text{ nm} \times 0.5 \text{ nm}$ samples for $\kappa = 1.1$. (b1)-(b3) Stable target skyrmions of $n_{max} = 5, 8$ and 12 in $200 \text{ nm} \times 400 \text{ nm} \times 0.5 \text{ nm}$, $400 \text{ nm} \times 800 \text{ nm} \times 0.5 \text{ nm}$ and $600 \text{ nm} \times 1200 \text{ nm}$ samples for $\kappa = 1.1$. (c1)-(c3) Stable target skyrmions of $n_{max} = 5, 9$ and 13 in $200 \text{ nm} \times 200 \text{ nm} \times 0.5 \text{ nm}$, $400 \text{ nm} \times 400 \text{ nm} \times 0.5 \text{ nm}$ and $600 \text{ nm} \times 600 \text{ nm} \times 0.5 \text{ nm}$ samples for $\kappa = 4$. (d1)-(d3) Stable target skyrmions of $n_{max} = 5, 10$ and 14 in $200 \text{ nm} \times 400 \text{ nm} \times 0.5 \text{ nm}$, $400 \text{ nm} \times 800 \text{ nm} \times 0.5 \text{ nm}$ and $600 \text{ nm} \times 1200 \text{ nm}$ for $\kappa = 4$. Insets of (a1)-(d3) are initial configurations. (e)-(f) Spin profiles of stripes. The symbols are numerical data and the solid lines are the fits to $\cos \Theta(x) = -\frac{\sinh^2(L/2w) - \sinh^2(x/w)}{\sinh^2(L/2w) + \sinh^2(x/w)}$ for $-L/2 < x < L/2$ and $\cos \Theta(x) = \frac{\sinh^2(L/2w) - \sinh^2[(x-L)/w]}{\sinh^2(L/2w) + \sinh^2[(x-L)/w]}$ for $L/2 < x < 3L/2$ with $L = 32.50$ nm and $w = 5.23$ nm (e); and $L = 25.10$ nm and $w = 7.63$ nm (f). Color bar denotes skyrmion charge density and the gray-scale encodes m_z .

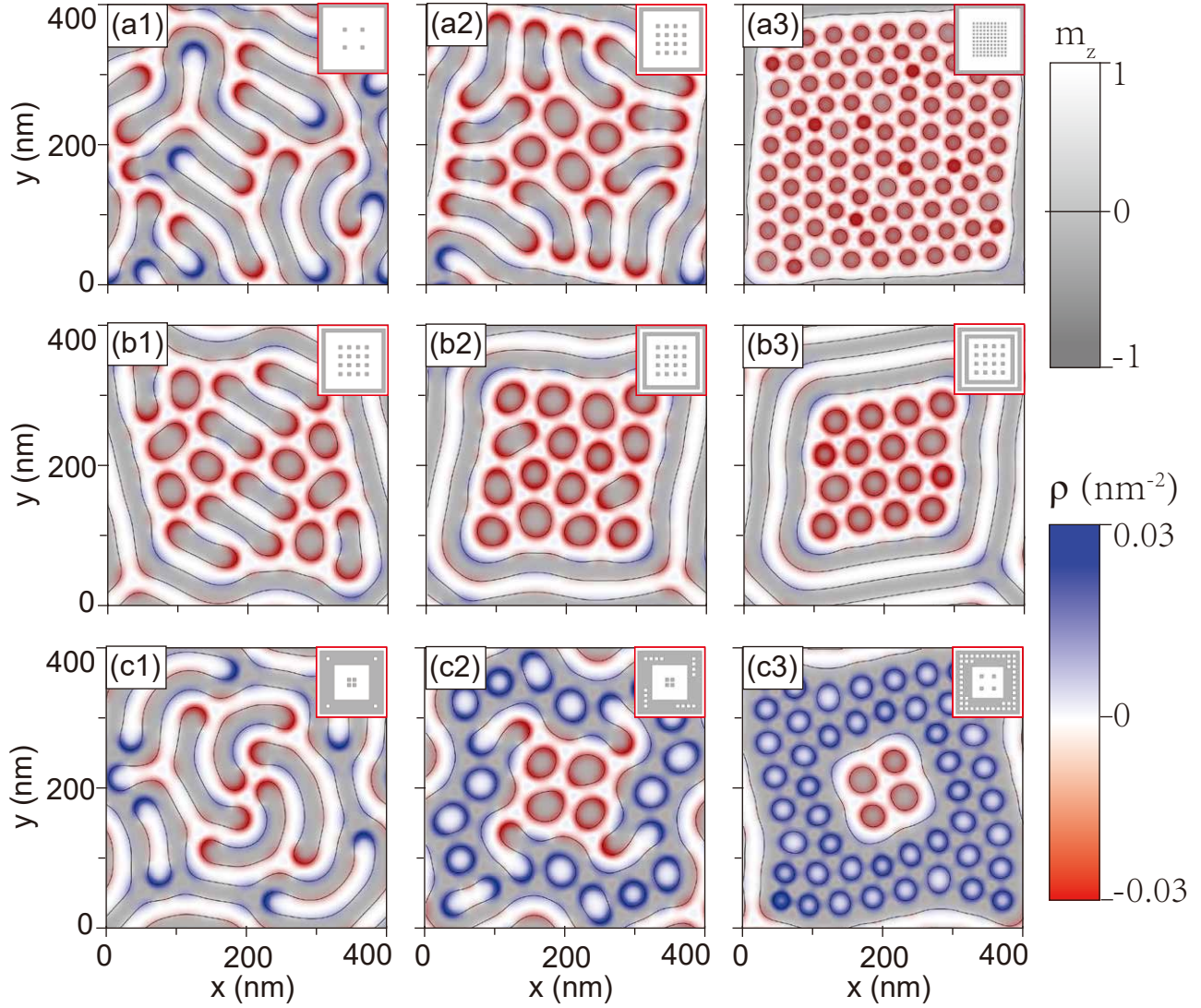


FIG. 7. Morphology and structures of various stable cascade stripe skyrmion bags for $\kappa = 4$. (a1)-(a3) Stripe skyrmion bags of $n = 2$ with $N = 4$ (a1), 16 (a2) and 100 (a3) skyrmions in the innermost bag. (b1)-(b3) Cascade stripe skyrmion bags of $n = 3$ (b1), 4 (b2) and 5 (b3) with $N = 16$ skyrmions in the innermost bag. (c1)-(c3) Cascade stripe skyrmion bags of $n = 3$ with $N = 4$ skyrmions in the innermost bag and 4 skyrmions (c1), 16 skyrmions (c2), and 36 skyrmions (c3) in the next innermost bag. Insets are the initial configurations of these cascade stripe skyrmion bags. Color bar denotes skyrmion charge density and the gray-scale encodes m_z .

ible and irregular in order to fill up the film as shown in Figs. 1(b1)-(b3). Their widths should be resilient to cascade structures no matter whether they are in a single stripe skyrmion, or a target stripe skyrmion, or in a cascade stripe skyrmion bags, as long as the distance between two cascade layers are larger than the fundamental stripe width of $a(\kappa)2\pi A/D$. Figure 5 shows stable target stripe skyrmions of $n = 4, 6$ and 8 layers in a sample of $600 \text{ nm} \times 600 \text{ nm} \times 0.5 \text{ nm}$ for $\kappa = 1.1$ (a1)-(a3) and $\kappa = 4$ (b1)-(b3). They are generated from the initial configurations shown in the insets of (a1)-(a3) for $n = 4, 6$, and 8, respectively. The reasons for using these initial configurations are the same for those in Fig. 1.

The average available layer space length of the target skyrmions are $600 \text{ nm}/(2 \times 4) = 75 \text{ nm}$ for Figs. 5(a1) and 5(b1), 50 nm for Figs. 5(a2) and 5(b2), and 37 nm for Figs. 5(a3) and 5(b3), larger than the elementary stripe width of $L = 32.5 \text{ nm}$ for $\kappa = 1.1$ and $L = 25.10 \text{ nm}$ for $\kappa = 4$. Spin profiles of stripes in all layers are the same as that for elementary stripes as shown in Figs. 5(c)-(d). The symbols are numerical data along the green lines labelled by the green \textcircled{n} in Figs. 5(a1)-(a3) for (c) and along the orange lines labelled by the orange \textcircled{n} in Figs. 5(b1)-(b3) for (d). The solid curves are the fit to $\cos \Theta(x) = -\frac{\sinh^2(L/2w) - \sinh^2(x/w)}{\sinh^2(L/2w) + \sinh^2(x/w)}$ for $-L/2 < x <$

$L/2$ and $\cos \Theta(x) = \frac{\sinh^2(L/2w) - \sinh^2[(x-L/2-L/2)/w]}{\sinh^2(L/2w) + \sinh^2[(x-L/2-L/2)/w]}$ for $L/2 < x < L/2 + L$ with $L = 32.50$ nm and $w = 5.2$ nm [Fig. 5(c)], and with $L = 25.10$ nm and $w = 7.6$ nm [Fig. 5(d)].

Different from the case of $\kappa < 1$, the number of layers of a stable target stripe skyrmion can be any value in the thermodynamic limit, and has a maximal value for a finite sample. The maximal number is slightly larger than the half of the ratio between the sample size and the elementary stripe width. Figures 6(a1)-(a3) are three stable target stripe skyrmions for $\kappa = 1.1$ with maximal layers of $n_{max} = 4, 8$ and 11 when the sample sizes are $200 \text{ nm} \times 200 \text{ nm} \times 0.5 \text{ nm}$, $400 \text{ nm} \times 400 \text{ nm} \times 0.5 \text{ nm}$ and $600 \text{ nm} \times 600 \text{ nm} \times 0.5 \text{ nm}$ for $\kappa = 1.1$, respectively. They are from the initial configurations shown in the insets of corresponding figures with more layers than their final stable values. Similar to the evolutions of those stable circular target skyrmions in Fig. 2, the extra layers shrink and disappear one by one from the sample center. n_{max} is very close to $200/(2 \times 32.5) = 3.15$; $400/(2 \times 32.5) = 6.3$; and $600/(2 \times 32.5) = 9.45$, corresponding to average available space size of 25 nm (a1), 25 nm (a2), and $\approx 27 \text{ nm}$ (a3). The general features do not depend on the sample shape. As shown in Figs. 6(b1)-(b3) for rectangular samples of $200 \text{ nm} \times 400 \text{ nm} \times 0.5 \text{ nm}$, $400 \text{ nm} \times 800 \text{ nm} \times 0.5 \text{ nm}$ and $600 \text{ nm} \times 1200 \text{ nm} \times 0.5 \text{ nm}$ with exactly the same model parameters of $\kappa = 1.1$ as those in Figs. 6(a1)-(a3). $n_{max} = 5$ (b1), 8 (b2), and 12 (b3) are mainly determined by the shorter length, and are similar to those in (a1)-(a3). Remarkably, the skyrmion in the innermost layer becomes a circular skyrmion of size 21 nm (a1), 10.3 nm (a2) and 14.5 nm (a3), much smaller than the elementary stripe width of $L = 32.5 \text{ nm}$. However, stripe width and spin profile in the outer layers are the same as the elementary stripes as shown in Fig. 6(e) with the symbols from the numerical simulations along the green lines labelled by the green \textcircled{n} in Fig. 6(b1)-(b3) and the solid curves from the fit to $\cos \Theta(x) = -\frac{\sinh^2(L_1/2w) - \sinh^2(x/w)}{\sinh^2(L/2w) + \sinh^2(x/w)}$ for $-L/2 < x < L/2$ and $\cos \Theta(x) = \frac{\sinh^2(L/2w) - \sinh^2[(x-L)/w]}{\sinh^2(L/2w) + \sinh^2[(x-L)/w]}$ for $L/2 < x < 3L/2$ with $L = 32.50$ nm and $w = 5.2$ nm.

To show that this feature is general for all $\kappa > 1$, Figs. 6(c1)-(c3) are three target stripe skyrmions with $n_{max} = 5, 9$ and 13 in $200 \text{ nm} \times 200 \text{ nm} \times 0.5 \text{ nm}$, $400 \text{ nm} \times 400 \text{ nm} \times 0.5 \text{ nm}$ and $600 \text{ nm} \times 600 \text{ nm} \times 0.5 \text{ nm}$ samples for $\kappa = 4$, respectively. Since the elementary stripe width is reduced to $L = 25.1 \text{ nm}$ for $\kappa = 4$, n_{max} increases slightly and is again slightly larger than the ratio of sample size to $2L$ that is $\simeq 4$ (c1), 8 (c2) and 12 (c3). Figures 6(d1)-(d3) are the stable target stripe skyrmions with the maximal layers of $n_{max} = 5, 10$ and 14 for rectangular samples of $200 \text{ nm} \times 400 \text{ nm} \times 0.5 \text{ nm}$, $400 \text{ nm} \times 800 \text{ nm} \times 0.5 \text{ nm}$ and $600 \text{ nm} \times 1200 \text{ nm} \times 0.5 \text{ nm}$, respectively, with exactly the same model parameters as those in Figs. 6(c1)-(c3). Again, the skyrmion in the innermost layer is a circular object of 5.73 nm (d1), 3.76 nm (d2) and 6.44 nm (d3) in diameter that is smaller than the elementary stripe

width of $L = 25.1 \text{ nm}$. Stripe width and spin profile in the outer layers are the same as the elementary stripes as shown in Fig. 6(f) with the symbols from the numerical simulations along the orange lines labelled by the orange \textcircled{n} in Figs. 6(d1)-(d3) and the solid curves from the fit to $\cos \Theta(x) = -\frac{\sinh^2(L_1/2w) - \sinh^2(x/w)}{\sinh^2(L/2w) + \sinh^2(x/w)}$ for $-L/2 < x < L/2$ and $\cos \Theta(x) = \frac{\sinh^2(L/2w) - \sinh^2[(x-L)/w]}{\sinh^2(L/2w) + \sinh^2[(x-L)/w]}$ for $L/2 < x < 3L/2$ with $L = 25.1 \text{ nm}$ and $w = 7.63 \text{ nm}$.

Figures 5 and 6 show clearly that stripes in all kinds of composite stripe skyrmions keep the properties of elementary stripe skyrmions, such as their widths and spin profiles, at low skyrmion density such that the distance between two neighbouring layers is larger than the elementary width. Naturally, one interesting question is what will happen to the structure and morphology of composite skyrmions when more skyrmions are added into one particular layer or several layers. From the fact that a collection of elementary stripe skyrmions form a SkX when the skyrmion-skyrmion distance is comparable to elementary stripe width [46, 47], one expects that highly irregularly arranged flexible stripes of well-defined width as shown in Fig. 7(a1) deform their shapes to circular objects when the mean skyrmion-skyrmion distance inside one particular bag is reduced, and they eventually form SkXs in the layer(s) when the distance is around $L = a(\kappa)2\pi A/D$. Figure 7 shows morphology change of cascade stripe skyrmions bags of various layers n and $\kappa = 4$ when the number of skyrmions in the innermost and next innermost bags increase from a low skyrmion density to a higher skyrmion density in a sample of $400 \text{ nm} \times 400 \text{ nm} \times 0.5 \text{ nm}$. Figures 7(a1)-(a3) are the stable cascade stripe skyrmion bags of $n = 2$ with $N = 4$ (a1), 16 (a2), and 100 (a3) skyrmions in the innermost bag. Skyrmions in the innermost bag are highly irregular stripes when the skyrmion density is low, as shown in Fig. 7(a1). It becomes a mixture of 4 circular skyrmions and 12 short straight stripe skyrmions when the average skyrmion-skyrmion distance is around $\sqrt{(400 - 2 \times 25.10)^2/16}/2 \approx 44 \text{ nm} \simeq 1.8L$ as shown in Fig. 7(a2). 100 skyrmions in the innermost bag for a nice triangular crystal as shown in Fig. 7(a3) when the average skyrmion-skyrmion distance is around $0.7L$. Figures 7(b1)-(b3) are the stable cascade stripe skyrmion bags of $n = 3$ (b1), 4 (b2) and 5 (b3) with $N = 16$ skyrmions in the innermost bag. The bag size decreases as n increases such that the effective skyrmion density in the bag increases. The 16 skyrmions form a mixture of circular and stripe skyrmions (b1), a SkX-like structure (b2), and an almost perfect SkX (b3). Figures 7(c1)-(c3) are cascade stripe skyrmion bags of $n = 3$ with $N = 4$ skyrmions in the innermost bag and 4 skyrmions (c1), 16 skyrmions (c2), and 36 skyrmions (c3) in the next innermost bag. When skyrmion densities in both bags are low, 4 skyrmions in both bags are irregular stripes as shown in (c1). Skyrmions in both bags are circular when the average skyrmion-skyrmion distance is around elementary stripe width as shown in (c2). Skyrmions in

both bags form triangular lattice structures when the effective skyrmion densities are high enough as shown in (c3).

IV. DISCUSSION AND CONCLUSION

It should be pointed out that many composite skyrmions discussed here were reported in previous micromagnetic simulations and in experiments. For example, skyrmionium were observed in space-coiling meta-structure [55], target skyrmions were observed in FeGe nanodisks [53], in space-coiling meta-structure [55], and in Pd/Fe/Ir hexagon systems[62], more exotic cascaded skyrmion bags were observed in liquid crystals [59], in $\text{Fe}_{3-x}\text{GeTe}_2$ [70], and in chiral nematic liquid crystals [71]. Here we propose a coherent way to organize these exotic skyrmion-like structures.

Composite skyrmions reveal fundamental nature of skyrmion duality. The duality allows all kinds of superstructures from elementary skyrmions, very similar to using bricks to construct different buildings in daily life. These superstructures provide countless new information carriers with distinct topologies and make new device concepts and new designs possible. For example, topology-based memory and gates should have high stability, high error tolerance and low noise [64–68]. Topologically protected particle can also find its applications in electro-optic, microfluidic, and nanoparticle transport [59, 69–71]. Charge and spin in solid state are coupled. Electron transport can be affected by the magnetic texture either through the emerged magnetic and electric fields, or simply through spin-orbit interactions. Thus, it should be highly interesting to identify those localized composite skyrmions which can be easily made on-demand, high controllability, and easily distinguish one from the others, especial electronically.

Composite skyrmions can be used for magnetic data storage due to high stability and topological protection. They can also be used as magnetic sensors due to their sensitivity to external magnetic fields[69]. Another possible application of composite skyrmions is in energy-efficient computing applications, such as low-power spintronic devices and neuromorphic computing due to their varieties in morphology huge number of accessible states such that they can emulate the behavior of neurons[74]. One may use composite skyrmions to generate spin currents, which can be used to control magnetization.

Although we did not consider magnetic field effect in this study, external magnetic fields can surely modify magnetic anisotropy that, in turn, can affect stability and properties of composite skyrmions[70]. Magnetic fields are surely an effective control knob. It should be very important and interesting to understand in detail how a magnetic field affects composite skyrmions, not only in terms of practical applications but also fundamentals,

In conclusion, topology and static properties of stable/metastable magnetic textures of chiral magnets in

the absence of magnetic field are fully determined by parameter κ , which measures relative strength of chiral interaction to the ferromagnetic exchange interaction and anisotropy, not by individual material parameters. $L = 4A/(\pi D)$ is the fundamental length scale of all possible magnetic structures in a chiral magnet. Skyrmions have particle-continuum-medium duality that results in various interesting composite skyrmions such as target skyrmions and skyrmion bags. The complexities and the maximal number of cascade layers of a skyrmion superstructure with a given topology is sensitive to value of κ for $\kappa \leq 1$ which support isolated circular skyrmions. For chiral magnetic films of $\kappa > 1$, where condensed stripe skyrmions is the thermodynamic equilibrium state at finite temperature, cascade stripe skyrmions maintain the width of elementary stripe skyrmions as long as the space between two cascade layers is larger than the width of elementary stripe skyrmions. When the space between two cascade layers is less than the fundamental stripe width, the cascade stripe skyrmions tend to be unstable. In the case of inserting many skyrmions inside one particular layer, whether in the innermost layer or any other cascade layer, such that the average skyrmion-skyrmion distance in around the fundamental stripe width, skyrmions because circular and form a triangular SkX. Our findings open the possibilities of new concepts and new designs in applications.

ACKNOWLEDGMENTS

This work is supported by the National Key Research and Development Program of China (No. 2020YFA0309600), the NSFC Grant (No. 11974296), and Hong Kong RGC Grants (No. 16301619, 16300522, and 16302321).

Appendix A: Evidences of structure determination by κ

The putative assertion from Eq. (3) is that (meta)stable spin structures are completely determined by κ up to a proper scaling is a sweet surprising. In order to further confirm this assertion, we use a film of $400\text{ nm} \times 400\text{ nm} \times 0.5\text{ nm}$ described by Eq. (1) to simulate various metastable structures with the same κ and different A/D . We set $\kappa = 4$ that supports condensed stripe skyrmions and with 10 nucleation domain randomly distributed in the film. Initially, the model parameters are $A = 1\text{ pJ m}^{-1}$, $D = 1\text{ mJ m}^{-2}$, $K_u = 0.154\text{ MJ m}^{-3}$, $M_s = 0.58\text{ MA m}^{-1}$. Figure 8(a) below shows the morphology of the final stable structure with 10 ramified stripe skyrmions. Then we gradually increase A/D from 1 nm to 5 nm and decrease K_u to keep the $\kappa = 4$ unchanged, and Figs. 8(b)-(e) are the final stable structures for $A/D = 2\text{ nm}$ (b); 3 nm (c); 4 nm (d); 5 nm (e). Although these structures are visually different, showing

multiply solutions of Eq. (3), they are in fact similar. Fig. 8(f) plot $M_z(x)$ along the green lines labelled by

①-⑤ in Figs. 8(a)-(e). The spin profiles fall on the same curve when x is plotted in the units of A/D . The results are exactly what the assertion is expected.

-
- [1] A. N. Bogdanov and U. K. Röbber, Chiral Symmetry Breaking in Magnetic Thin Films and Multilayers, *Phys. Rev. Lett.* **87**, 037203 (2001).
- [2] U. K. Röbber, A. N. Bogdanov, and C. Pfeiderer, Spontaneous skyrmion ground states in magnetic metals, *Nature* **442**, 797 (2006).
- [3] S. Mühlbauer, B. Binz, F. Jonietz, C. Pfeiderer, A. Rosch, A. Neubauer, G. Georgii, and P. Böni, Skyrmion lattice in a chiral magnet, *Science* **323**, 915 (2009).
- [4] X. Z. Yu, Y. Onose, N. Kanazawa, J. H. Park, J. H. Han, Y. Matsui, N. Nagaosa, and Y. Tokura, Real-space observation of a two-dimensional skyrmion crystal, *Nature* **465**, 901 (2010).
- [5] X. Z. Yu, N. Kanazawa, Y. Onose, K. Kimoto, W. Z. Zhang, S. Ishiwata, Y. Matsui, and Y. Tokura, Near room-temperature formation of a skyrmion crystal in thin-films of the helimagnet FeGe, *Nat. Mater.* **10**, 106 (2011).
- [6] N. Nagaosa and Y. Tokura, Topological properties and dynamics of magnetic skyrmions, *Nat. Nanotech.* **8**, 899 (2013).
- [7] A. Fert, V. Cros, and J. Sampaio, Skyrmions on the track, *Nat. Nanotech.* **8**, 152 (2013); J. Sampaio, V. Cros, S. Rohart, A. Thiaville, and A. Fert, Nucleation, stability and current-induced motion of isolated magnetic skyrmions in nanostructures, *ibid.* **8**, 839 (2013).
- [8] N. Romming, C. Hanneken, M. Menzel, J. E. Bickel, B. Wolter, K. von Bergmann, A. Kubetzka, and R. Wiesendanger, Writing and deleting single magnetic skyrmions, *Science* **341**, 636 (2013).
- [9] X. S. Wang, H. Y. Yuan, and X. R. Wang, A theory on skyrmion size, *Commun. Phys.* **1**, 31 (2018).
- [10] J. Li, A. Tan, K. W. Moon, A. Doran, M. A. Marcus, A. T. Young, E. Arenholz, S. Ma, R. F. Yang, C. Hwang *et al.*, Tailoring the topology of an artificial magnetic skyrmion, *Nat. Commun.* **5**, 4704 (2014).
- [11] H. Y. Yuan and X. R. Wang, Skyrmion Creation and Manipulation by Nano-Second Current Pulses, *Sci. Rep.* **6**, 22638 (2016).
- [12] Y. Zhou and M. A. Ezawa, A reversible conversion between a skyrmion and a domain-wall pair in a junction geometry, *Nat. Commun.* **5**, 4652 (2014).
- [13] W. Jiang, P. Upadhyaya, W. Zhang, G. Yu, M. B. Jungfleisch, F. Y. Fradin, J. E. Pearson, Y. Tserkovnyak, K. L. Wang, O. Heinonen *et al.*, Blowing magnetic skyrmion bubbles, *Science* **349**, 283 (2015).
- [14] H. Du, R. Che, L. Kong, X. Zhao, C. Jin, C. Wang, J. Yang, W. Ning, R. Li, C. Jin *et al.*, Edge-mediated skyrmion chain and its collective dynamics in a confined geometry, *Nat. Commun.* **6**, 8504 (2015).
- [15] Y. Onose, Y. Okamura, S. Seki, S. Ishiwata, and Y. Tokura, Observation of magnetic excitations of skyrmion crystal in a helimagnetic insulator Cu_2OSeO_3 , *Phys. Rev. Lett.* **109**, 037603 (2012).
- [16] H. S. Park, X. Z. Yu, S. Aizawa, T. Tanikaki, T. Akashi, Y. Takahashi, T. Matsuda, N. Kanazawa, Y. Onose, D. Shindo *et al.*, Observation of the magnetic flux and three-dimensional structure of skyrmion lattices by electron holography, *Nat. Nanotech.* **9**, 337 (2014).
- [17] X. Gong, H. Y. Yuan, and X. R. Wang, Current-driven skyrmion motion in granular films, *Phys. Rev. B* **101**, 064421 (2020).
- [18] S. Heinze, K. von Bergmann, M. Menzel, J. Brede, A. Kubetzka, R. Wiesendanger, G. Bihlmayer, and Stefan Blügel, Spontaneous atomic-scale Magnetic skyrmion lattice in two dimensions, *Nat. Phys.* **7**, 713 (2011).
- [19] S. Krause and R. Wiesendanger, Spintronics: Skyrmionics gets hot, *Nat. Mater.* **15**, 493 (2016).
- [20] P. Dürrenfeld, Y. Xu, J. Åkerman, and Y. Zhou, Controlled skyrmion nucleation in extended magnetic layers using a nanocontact geometry, *Phys. Rev. B* **96**, 054430 (2017).
- [21] H. Y. Yuan, X. S. Wang, Man-Hong Yung, and X. R. Wang, Wiggling skyrmion propagation under parametric pumping, *Phys. Rev. B* **99**, 014428 (2019).
- [22] S. Rohart and A. Thiaville, Skyrmion confinement in ultrathin film nanostructures in the presence of Dzyaloshinskii-Moriya interaction, *Phys. Rev. B* **88**, 184422 (2013).
- [23] M. N. Wilson, A. B. Butenko, A. N. Bogdanov, and T. L. Monchesky, Chiral skyrmions in cubic helimagnet films: The role of uniaxial anisotropy, *Phys. Rev. B* **89**, 094411 (2014).
- [24] N. Romming, A. Kubetzka, C. Hanneken, K. von Bergmann, and R. Wiesendanger, Field-Dependent Size and Shape of Single Magnetic Skyrmions, *Phys. Rev. Lett.* **114**, 177203 (2015).
- [25] N. Vidal-Silva, A. Riveros, and J. Escrig, Stability of Néel skyrmions in ultra-thin nanodots considering Dzyaloshinskii-Moriya and dipolar interactions, *J. Magn. Magn. Mater.* **443**, 116 (2017).
- [26] A. O. Leonov, T. L. Monchesky, N. Romming, A. Kubetzka, A. N. Bogdanov, and R. Wiesendanger, The properties of isolated chiral skyrmions in thin magnetic films., *New J. Phys.* **18**, 065003 (2016).
- [27] H.-B. Braun, Fluctuations and instabilities of ferromagnetic domain-wall pairs in an external magnetic field, *Phys. Rev. B* **50**, 16485 (1994).
- [28] A. Siemens, Y. Zhang, J. Hagemeyer, E. Y. Vedmedenko, and R. Wiesendanger, Minimal radius of magnetic skyrmions: statics and dynamics, *New. J. Phys.* **18**, 045021 (2016).
- [29] E. Simon, K. Palotás, L. Rózsa, L. Udvardi, and L. Szunyogh, Formation of magnetic skyrmions with tunable properties in PdFe bilayer deposited on Ir(111), *Phys. Rev. B* **90**, 094410 (2014).
- [30] S. Jaiswal, K. Litzius, I. Lemes, F. Büttner, S. Finizio, J. Raabe, M. Weigand, K. Lee, J. Langer, B. Ocker *et al.*, Investigation of the Dzyaloshinskii-Moriya interaction and room temperature skyrmions in W/CoFeB/MgO thin films and microwires, *Appl. Phys. Lett.* **111**, 022409 (2017).

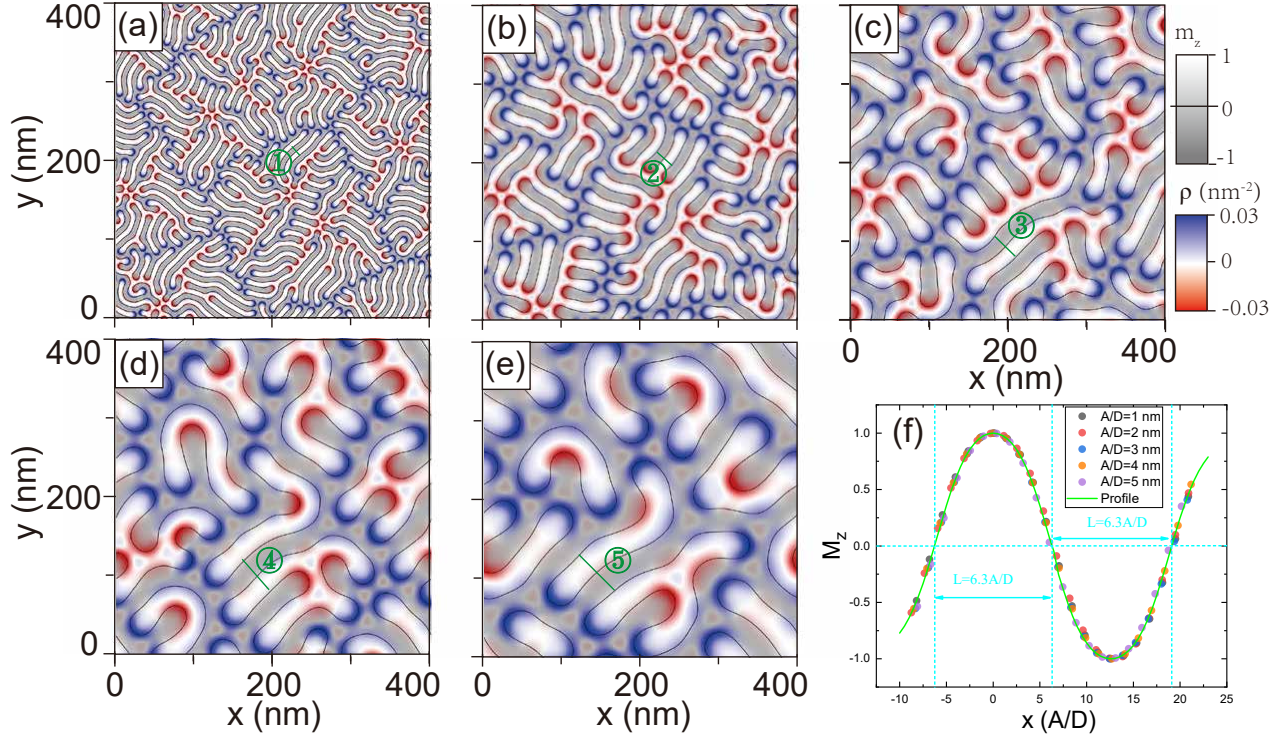


FIG. 8. (a)-(e) The structure of final state when $A/D=1$ nm (a); 2 nm (b); 3 nm (c); 4 nm (d); 5 nm (e). The inset of (a) shows the structure of the initial state. (f) The Spin profiles along the green lines labelled by ①-⑤ in (a)-(e). The symbols are numerical data and the solid lines are the theoretical fits to $M_z(x) = \frac{\sinh^2(L/w) - \sinh^2(x/2w)}{\sinh^2(L/w) + \sinh^2(x/2w)}$ for $-L/2 < x < L/2$ and $M_z(x) = \frac{\sinh^2[(x-L)/2w] - \sinh^2(L/w)}{\sinh^2(L/w) + \sinh^2[(x-L)/2w]}$ for $L/2 < x < 3L/2$.

- [31] E. A. Karhu, U. K. Rößler, A. N. Bogdanov, S. Kawaji, B. J. Kirby, H. Fritzsche, M. D. Robertson, C. F. Majkrzak, and T. L. Monchesky, Chiral modulations and reorientation effects in MnSi thin films, *Phys. Rev. B* **85**, 094429 (2012).
- [32] K. Litzius, I. Lemesh, B. Krüger, P. Bassirian, L. Caretta, K. Richter, F. Büttner, K. Sato, O. A. Tretiakov, J. Förster *et al.*, Skyrmion Hall effect revealed by direct time-resolved X-ray microscopy, *Nat. Phys.* **13**, 170 (2017).
- [33] S. Woo, K. Litzius, B. Krüger, M.-Y. Im, L. Caretta, K. Richter, M. Mann, A. Krone, R. M. Reeve, M. Weigand *et al.*, Observation of room-temperature magnetic skyrmions and their current-driven dynamics in ultrathin metallic ferromagnets, *Nat. Mater.* **15**, 501 (2016).
- [34] J. Iwasaki, M. Mochizuki, and N. Nagaosa, Universal current-velocity relation of skyrmion motion in chiral magnets, *Nat. Commun.* **4**, 1463 (2013).
- [35] C. Reichhardt, D. Ray, and C. J. Olson Reichhardt, Collective Transport Properties of Driven Skyrmions with Random Disorder, *Phys. Rev. Lett.* **114**, 217202 (2015).
- [36] C. Reichhardt and C. J. Olson Reichhardt, Noise fluctuations and drive dependence of the skyrmion Hall effect in disordered systems, *New J. Phys.* **18**, 095005 (2016).
- [37] J. Sampaio, V. Cros, S. Rohart, A. Thiaville, and A. Fert, Nucleation, stability and current-induced motion of isolated magnetic skyrmions in nanostructures, *Nat. Nanotech.* **8**, 839 (2013).
- [38] S.-Z. Lin, C. Reichhardt, C. D. Batista, and A. Saxena, Particle model for skyrmions in metallic chiral magnets: Dynamics, pinning, and creep, *Phys. Rev. B* **87**, 214419 (2013).
- [39] W. Koshibae and N. Nagaosa, Theory of current-driven skyrmions in disordered magnets, *Sci. Rep.* **8**, 6238 (2018).
- [40] R. Juge, S.-G. Je, D. de Souza Chaves, S. Pizzini, L. D. Buda-Prejbeanu, L. Aballe, M. Foerster, A. Locatelli, T. O. Menten, A. Sala *et al.*, Magnetic skyrmions in confined geometries: Effect of the magnetic field and the disorder, *J. Magn. Magn. Mater.* **455**, 3 (2018).
- [41] J.-V. Kim and M. -W. Yoo, Current-driven skyrmion dynamics in disordered films, *Appl. Phys. Lett.* **110**, 132404 (2017).
- [42] S. Hoshino and N. Nagaosa, Theory of the magnetic skyrmion glass, *Phys. Rev. B* **97**, 024413 (2018).
- [43] S. Woo, K. M. Song, X. Zhang, Y. Zhou, M. Ezawa, X. Liu, S. Finizio, J. Raabe, N. J. Lee, S.-I. Kim *et al.*, Current-driven dynamics and inhibition of the skyrmion Hall effect of ferrimagnetic skyrmions in GdFeCo films, *Nat. Commun.* **9**, 959 (2018).
- [44] X. R. Wang, X. C. Hu, and H. T. Wu, Stripe skyrmions and skyrmion crystals, *Commun. Phys.* **4**, 142 (2021).
- [45] H. T. Wu, X. C. Hu, K. Y. Jing, and X. R. Wang, Size and profile of skyrmions in skyrmion crystals, *Commun. Phys.* **4**, 210 (2021).

- [46] H. T. Wu, X. C. Hu, and X. R. Wang, Nematic and smectic stripe phases and stripe-SkX transformations, *Science China* **65**, 247512 (2022).
- [47] X. C. Hu, H. T. Wu, and X. R. Wang, A theory of skyrmion crystal formation, *Nanoscale* **14**, 7516 (2022).
- [48] X. R. Wang, X. C. Hu, and Z. Z. Sun, Topological Equivalence of Stripy States and Skyrmion Crystals, *Nano Letters* (in press), (2023).
- [49] A. O. Leonov, U. K. Rößler, and M. Mostovoy, Target-skyrmions and skyrmion clusters in nanowires of chiral magnets, *EDP Sciences* **75**, 05002 (2014).
- [50] X. Zhang, J. Xia, Y. Zhou, D. Wang, X. Liu, W. Zhao, and M. Ezawa, Control and manipulation of a magnetic skyrmionium in nanostructures, *Phys. Rev. B* **94**, 094420 (2016).
- [51] S. Zhang, F. Kronast, G. van der Laan, and T. Hesjedal, Real-space observation of skyrmionium in a ferromagnet-magnetic topological insulator heterostructure, *Nano Lett.* **18**, 1057 (2018).
- [52] M. M. M. Bhukta, M. Abhilash, P. Gajanan, M. Sougata, B. S. Braj, and B. Subhankar, A novel chiral spin texture: Antiferromagnetic Skyrmionium, *arXiv* 1810.08262, (2018).
- [53] F. Zheng, H. Li, S. Wang, D. Song, C. Jin, W. Wei, A. Kovács, J. Zang, M. Tian, Y. Zhang *et al.*, Direct imaging of a zero-field target skyrmion and its polarity switch in a chiral magnetic nanodisk, *Phys. Rev. Lett.* **119**, 197205 (2017).
- [54] Y. Zhang, C. Xu, P. Chen, Y. Nahas, S. Prokhorenko, and L. Bellaiche, Emergence of skyrmionium in a two-dimensional CrGe(Se, Te)₃ Janus monolayer, *Phys. Rev. B* **102**, 241107 (2020).
- [55] Z. L. Deng, T. Shi, A. Krasnok, X. P. Li, and A. Alú, Observation of localized magnetic plasmon skyrmions, *Nat. Commun.* **13**, 1 (2022).
- [56] A. G. Kolesnikov, M. E. Stebliy, A. S. Samardak, and A. V. Ognev, Skyrmionium—high velocity without the skyrmion Hall effect, *Sci. Rep.* **8**, 1 (2018).
- [57] L. Shen, X. Li, Y. Zhao, J. Xia, G. P. Zhao, and Y. Zhou, Current-induced dynamics of the antiferromagnetic skyrmion and skyrmionium, *Phys. Rev. Appl.* **12**, 064033 (2019).
- [58] S. Li, J. Xia, X. Zhang, M. Ezawa, W. Kang, X. X. Liu, Y. Zhou, and W. S. Zhao, Dynamics of a magnetic skyrmionium driven by spin waves, *Appl. Phys. Lett.* **112**, 142404 (2018).
- [59] D. Foster, C. Kind, P. J. Ackerman, J. -S. B. Tai, M. R. Dennis, and I. I. Smalyukh, Two-dimensional skyrmion bags in liquid crystals and ferromagnets, *Nat. Phys.* **15**, 655 (2019).
- [60] J. Tang, L. Kong, Y. Wu, W. Wang, Y. Chen, Y. Wang, J. Li, Y. Soh, Y. Xiong, M. Tian *et al.*, Target bubbles in Fe₃Sn₂ nanodisks at zero magnetic field, *ACS Nano* **14**, 10986 (2020).
- [61] X. Shen, R. Zhao, L. Ji, C. Hu, W. Ren, W. Chen, Y. Li, J. Zhang, X. Zhang, and X. Dong, Breaking the topological protection of target skyrmions by the excitation of spin wave modes under microwave magnetic field, *J. Magn. Magn. Mater.* **541**, 168521 (2022).
- [62] D. Cortés-Ortuño, N. Romming, M. Beg, K. v. Bergmann, A. Kubetzka, O. Hovorka, H. Fangohr, and R. Wiesendanger, Nanoscale magnetic skyrmions and target states in confined geometries, *Phys. Rev. B* **99**, 214408 (2019).
- [63] C. Kind, S. Friedemann, and D. Read, Existence and stability of skyrmion bags in thin magnetic films, *Appl. Phys. Lett.* **116**, 022413 (2020).
- [64] J. Tang, Y. D. Wu, W. W. Wang, L. Y. Kong, B. Y. Lv, W. S. Wei, J. D. Zang, M. L. Tian, and H. F. Du, Magnetic skyrmion bundles and their current-driven dynamics, *Nature Nanotech.* **16**, 1086 (2021).
- [65] C. Kind and D. Foster, Magnetic skyrmion binning, *Phys. Rev. B* **103**, L100413 (2023).
- [66] Z. Zhang, M. Xua, G. Jiang, J. Zhang, D. Meng, W. Chen, Y. Chen, and C. Hu, High-density racetrack memory based on magnetic skyrmion bags controlled by voltage gates, *J. Appl. Phys.* **132**, 113901 (2022).
- [67] A. O. Leonov, Clusters and chains in bulk and thin-layered cubic helimagnets, *Phys. Rev. B* **105**, 094404 (2022).
- [68] R. Chen and Y. Li, Voltage-Controlled Skyrmionic Interconnect with Multiple Magnetic Information Carriers, *ACS Appl. Mater. Interfaces* **14**, 30420 (2022).
- [69] T. K. Bhowmick, A. De, and R. K. Lake, High figure of merit magneto-optics from interfacial skyrmions on topological insulator, *Phys. Rev. B* **98**, 024424 (2018).
- [70] L. Powalla, M. T. Birch, K. Litzius, S. Wintz, F. S. Yasin, L. A. Turnbull, F. Schulz, D. A. Mayoh, G. Balakrishnan, M. Weigand *et al.*, Seeding and Emergence of Composite Skyrmions in a van der Waals Magnet, *Adv. Mater.* 2208930 (2023).
- [71] Y. Shen and I. Dierking, Electrically driven formation and dynamics of skyrmionic solitons in chiral nematics, *Phys. Rev. Appl.* **15**, 054023 (2023).
- [72] A. Vansteenkiste, J. Leliaert, M. Dvornik, M. Helsen, F. Garcia-Sanchez, and F. B. V. Waeyenberge, The design and verification of MuMax3, *AIP Adv.* **4**, 107133 (2014).
- [73] A. Soumyanarayanan, M. Raju, A. L. Gonzalez Oyarce, A. K. C. Tan, M.-Y. Im, A. P. Petrović, P. Ho, K. H. Khoo, M. Tran, C. K. Gan, F. Ernult *et al.*, Tunable room-temperature magnetic skyrmions in Ir/Fe/Co/Pt multilayers, *Nature Mater.* **16**, 898 (2017).
- [74] K. M. Song, J.-S. Jeong, B. Pan, X. Zhang, J. Xia, S. Cha, T.-E. Park, K. Kim, S. Finizio, J. Raabe *et al.*, Skyrmion-based artificial synapses for neuromorphic computing, *Nat. Electron.* **3**, 148 (2020).